# Supplementary Materials

# Plasma-Wind-Assisted In₂S₃ Preparation with an Amorphous Surface Structure for Enhanced Photocatalytic Hydrogen Production

**Shaohui Guo [1], Hui Luo [2], Xiaochuan Duan [1], Bingqing Wei [3],\* and Xianming Zhang [4],\***

[1] College of Chemistry, Taiyuan University of Technology, Taiyuan 030024, China; guoshaohui@tyut.edu.cn (S.G.); duanxiaochuan@tyut.edu.cn (X.D.)

[2] Department of Chemical Engineering, Imperial College London, South Kensington Campus, London SW7 2AZ, UK; hui.luo@imperial.ac.uk

[3] Department of Mechanical Engineering, University of Delaware, Newark, DE 19716, USA

[4] Key Laboratory of Interface Science and Engineering in Advanced Material, Ministry of Education, Taiyuan University of Technology, Taiyuan 030024, China

\* Correspondence: weib@udel.edu (B.W.); zhangxianming@tyut.edu.cn (X.Z.)

### S1. Calculation of the Theoretical Photocurrents $J_{abs}$ of the Samples

The single photo energy is calculated from the following Equation:

$$E(\lambda) = h * \frac{C}{\lambda} \tag{S1}$$

where $E(\lambda)$ is the photo energy (J), $h$ is the Planck's constant ($6.626 \times 10^{-34}$ J s⁻¹), $C$ is the speed of light ($3 \times 10^8$ m s⁻¹), and $\lambda$ is the photon wavelength (nm).

The solar photon flux is calculated from the following Equation:

$$Flux(\lambda) = \frac{P(\lambda)}{E(\lambda)} \tag{S2}$$

where $Flux(\lambda)$ is the solar photon flux, and $P(\lambda)$ is the solar power flux (Reference Solar Spectral Irradiance: Air Mass 1.5. NREL. ASTM G-173 package. http://rredc.nrel.gov/solar/spectra/am1.5/ (accessed on 30 November 2021)).

The theoretical maximum photocurrent density under solar illumination, $J_{abs}$ is then calculated by integrating the solar photon flux as shown in the following Equation:

$$J_{abs} = e \times \int_{\lambda 2}^{\lambda 1} Flux(\lambda) d\lambda \tag{S3}$$

where $\lambda 1$ is the absorption edge of the sample according to Figure 4a, $\lambda 2$ is the lower limit of the measured solar spectrum, and $e$ is the elementary charge ($1.602 \times 10^{-19}$ C). The theoretical photocurrents of the In₂S₃ and P-In₂S₃ are accordingly calculated to be 0.51 and 0.85 mA cm⁻², respectively.

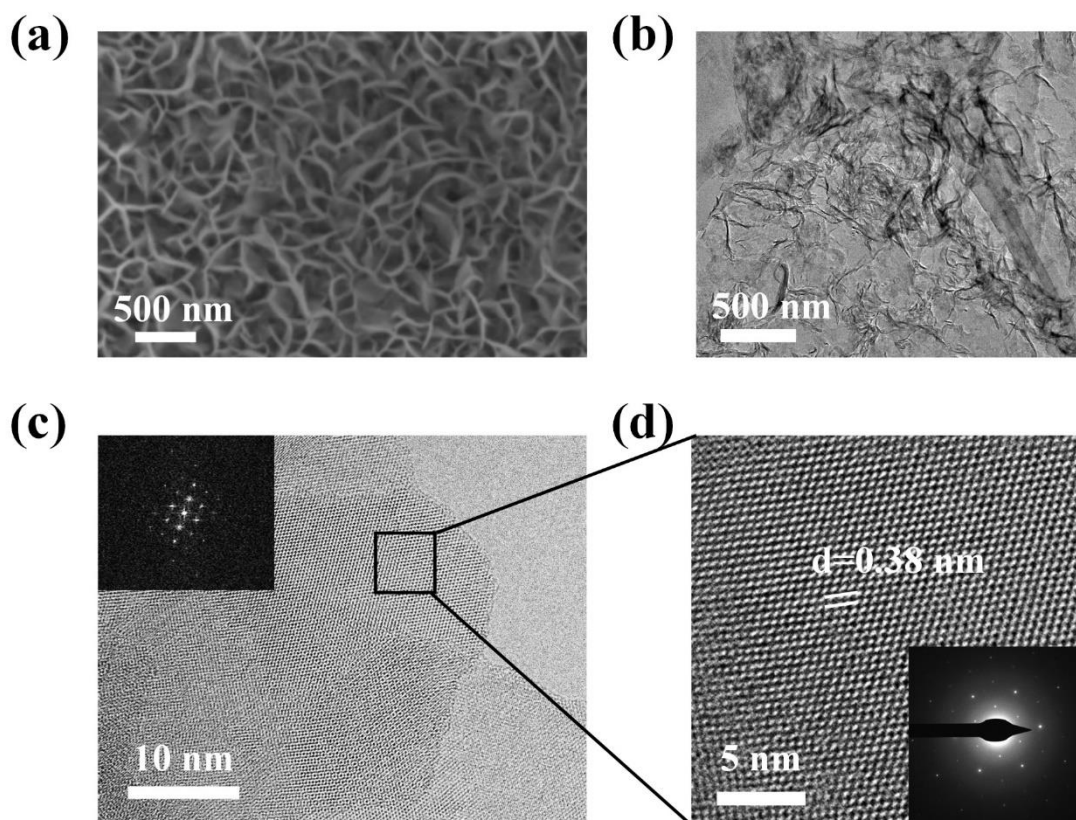**Figure S1.** (**a**) The SEM image, (**b**) the TEM image, and (**c**) the HRTEM image of the $In_2S_3$ sample. The inset is the Fourier transform of the black box area, and (**d**) the magnified HRTEM image of the $In_2S_3$ sample. The inset is the diffraction pattern of the sample.

The morphology of a bare $In_2S_3$ nanosheet is shown in Figure S1. Figure S1a shows a scanning electron micrograph (SEM) image of the sample, showing $In_2S_3$ nanosheets grown vertically on an FTO substrate, and the clear lines are the nanosheet edges. In Figure S1b, it is easily seen that the nanosheets are twisted like silk threads. In the high-resolution transmission electron microscopy image (Figure S1c and S1d), the crystal lattices of the sample can be seen, and their clean edges are focused on illustrating that a good crystal structure can be obtained. This is confirmed by the diffraction pattern of the sample $In_2S_3$ shown in Figure S1d.
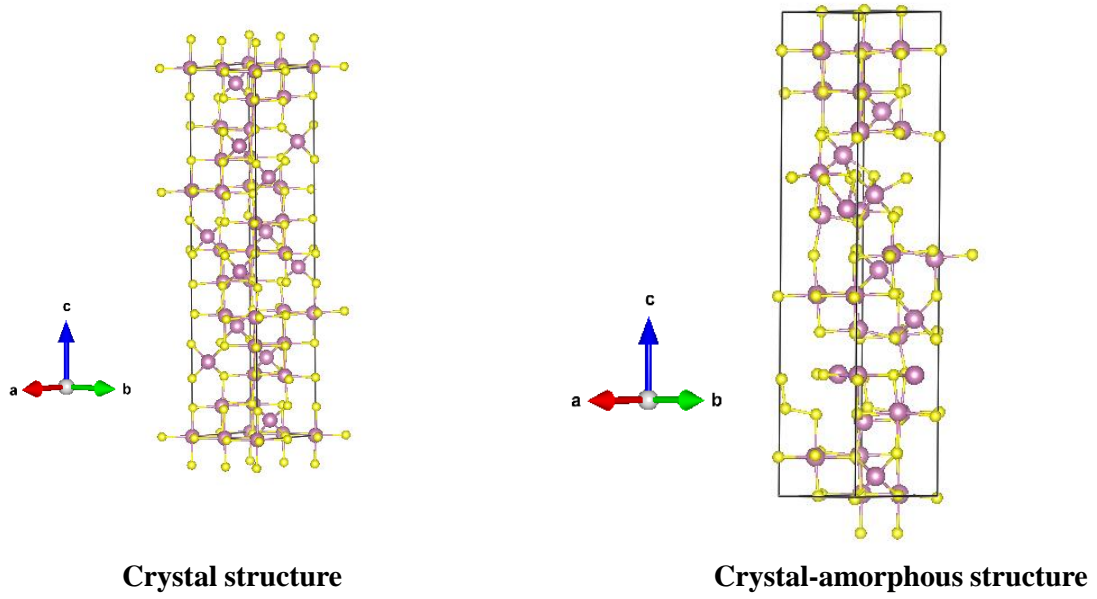
**Crystal structure**                    **Crystal-amorphous structure**

**Figure S2.** The material structures from the theoretical calculations. The yellow spheres are S atoms, and the purple spheres are In atoms.
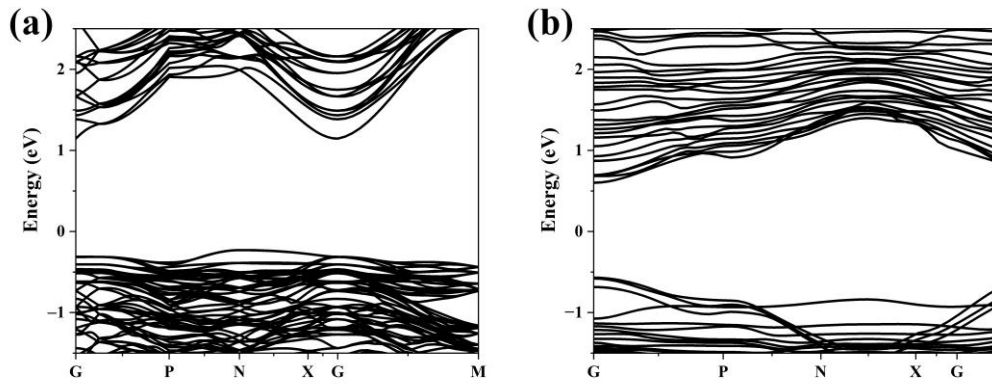


**Figure S3.** (**a**) The band structure of the crystal $In_2S_3$, (**b**) the band structure of the crystal-amorphous $In_2S_3$.
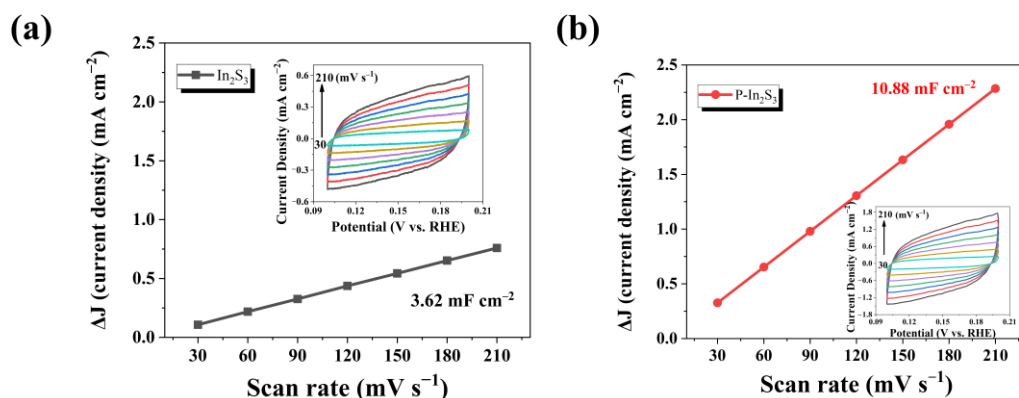
**Figure S4.** (**a**) Electrochemical active area of the In$_2$S$_3$. The inset is the CVs of the In$_2$S$_3$ with different scan rates and (**b**) the Electrochemical active area of the P-In$_2$S$_3$. The inset is the CVs of the P-In$_2$S$_3$ with varying scan rates.

In Figures S4a and S4b, the active electrochemical areas of the samples have been measured via the method of capacitive currents and different scan rates, where the scan rate varies from 30 mV s$^{-1}$ to 210 mV s$^{-1}$. The electrochemical surface area in bare In$_2$S$_3$ is about 3.62 mF cm$^{-2}$, whereas, with P-In$_2$S$_3$, the electrochemical surface area is 10.88 mF cm$^{-2}$, which favors hydrogen adsorption in a catalytic reaction.
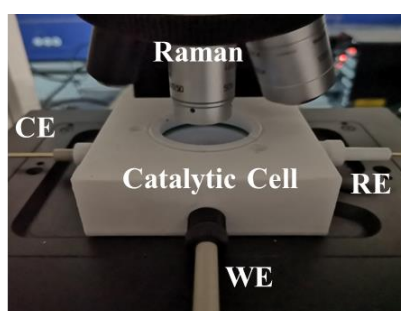


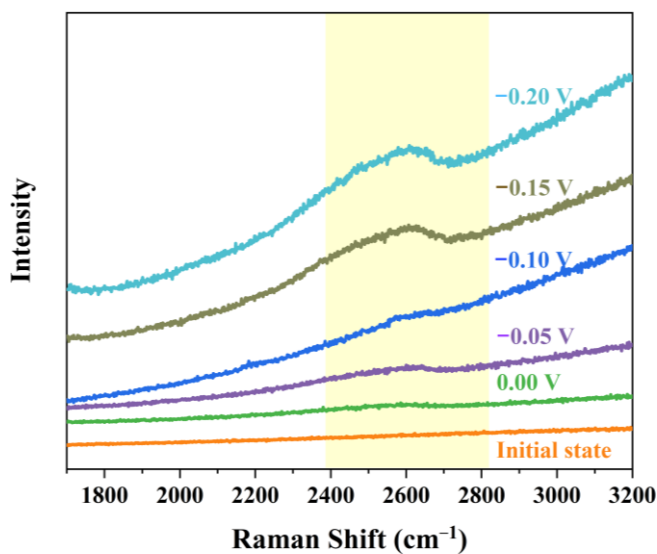**Figure S5.** The photo of the operando Raman measurement.



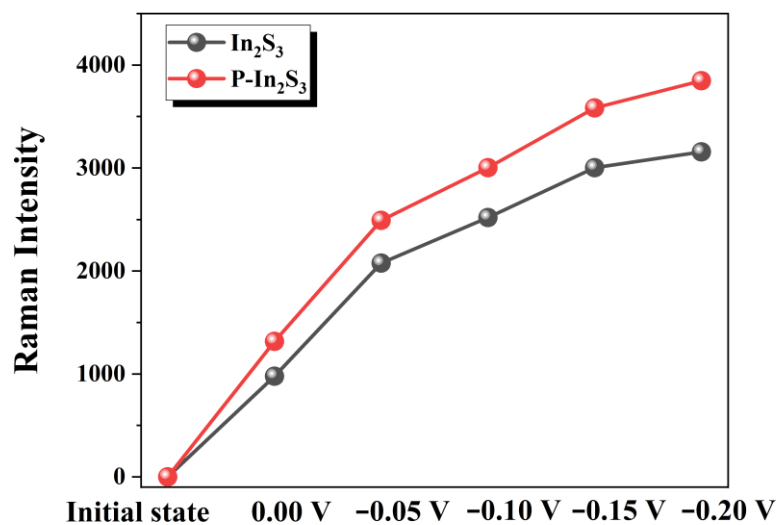**Figure S6.** The potential impact on the operando Raman intensity of the bare In$_2$S$_3$ sample.

**Figure S7.** The S–H bond Raman intensity after background subtraction versus the different potential during the operando Raman measurement.



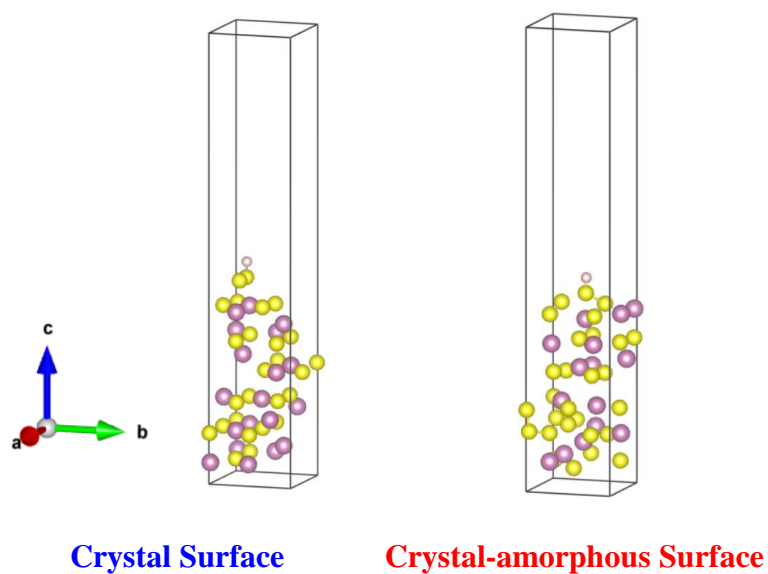**Crystal Surface**          **Crystal-amorphous Surface**

**Figure S8.** The hydrogen adsorption on the crystal surface and crystal-amorphous surface. The yellow spheres are S atoms, and the purple spheres are In atoms. The white sphere is the adsorption H atom.

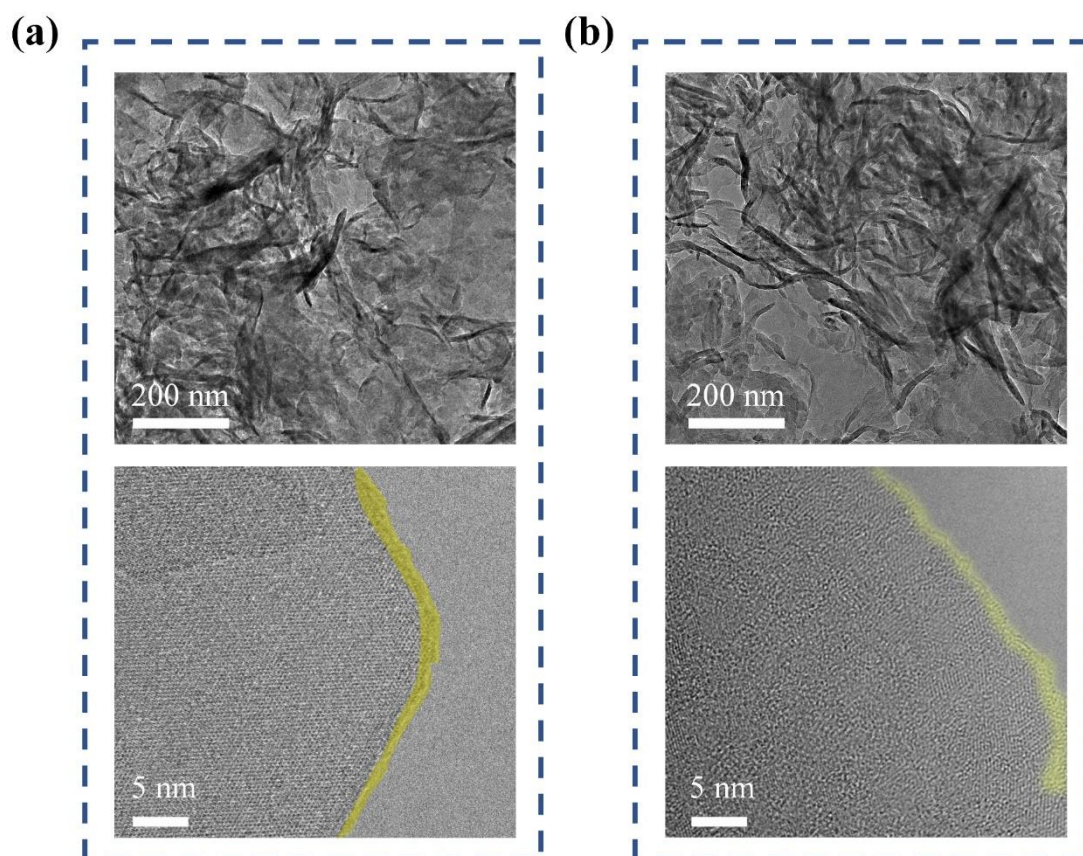**Figure S9.** The morphology of the sample after the catalytic reaction. (**a**) bare In2S3, (**b**) P-In2S3. It is noticed that the surface of the bare In2S3 has been destroyed through the HRTEM imaging; comparatively, the structure of the P-In2S3 is well maintained.
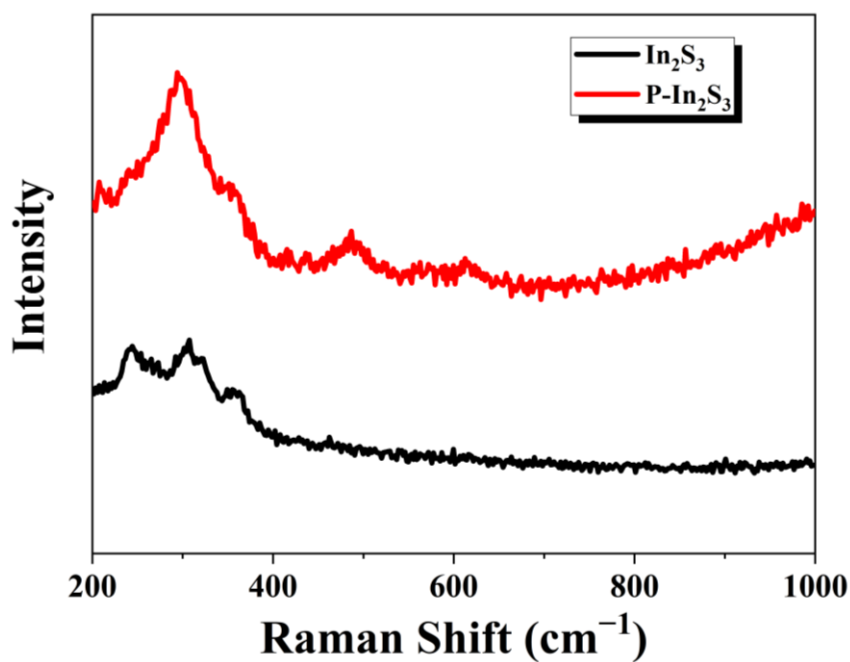


**Figure S10.** The Raman spectra of the P-In2S3 sample before and after the catalytic reaction.

**Table S1.** The comparison of hydrogen production rate, morphology, current density, and bandgap.

| Sample | Rate of $H_2$ Production | Morphology | Current Density | Bandgap | References |
|---|---|---|---|---|---|
| P-$In_2S_3$ | 457.35 $\mu mol\ cm^{-2}\ h^{-1}$ (3423.14 $\mu mol\ h^{-1}\ g^{-1}$) | surface amorphous nanosheets | 0.48 $mA\ cm^{-2}$ | 1.5 eV | this work |
| $MoS_2$@$In_2S_3$/$Bi_2S_3$ | 973.42 $\mu mol\ h^{-1}\ g^{-1}$ | core-shell heterojunction | 9 $\mu A\ cm^{-2}$ | - | [1] |
| $ZnIn_2S_4$-MIL-68/$In_2S_3$ | 306 $\mu mol\ h^{-1}\ g^{-1}$ | nanoparticles on microtubes | 0.64 $\mu A\ cm^{-2}$ | 2.38 eV | [2] |
| MoP/$In_2S_3$ | 481.73 $\mu mol\ h^{-1}\ g^{-1}$ | heterojunction | 1.7 $\mu A\ cm^{-2}$ | 2.01 eV | [3] |
| $Mo_2C$-$In_2S_3$ | 535.58 $\mu mol\ h^{-1}\ g^{-1}$ | heterojunction | 1.5 $\mu A\ cm^{-2}$ | - | [4] |
| $In_2S_3$-WC | 390.52 $\mu mol\ h^{-1}\ g^{-1}$ | flowers heterojunction | 1.8 $\mu A\ cm^{-2}$ | 1.88 eV | [5] |
| GO/$Fe_2P$/$In_2S_3$ | 483.35 $\mu mol\ h^{-1}\ g^{-1}$ | flowers heterojunction | - | - | [6] |
| $In_2S_3$/$ZnIn_2S_4$ | 12.1 $\mu mol\ cm^{-2}\ h^{-1}$ | nanosheets heterojunction | 1.06 $mA\ cm^{-2}$ | 2.0 eV | [7] |
| $Zn_mIn_2S_{m+3}$@$In_2S_3$ | 3300 $\mu mol\ h^{-1}\ g^{-1}$ | flowers heterojunction | 90 $\mu A\ cm^{-2}$ | - | [8] |

## References

1. Wang, Y.; Xing, Z.; Zhao, H.; Song, S.; Liu, M.; Li, Z.; Zhou, W. $MoS_2$@$In_2S_3$/$Bi_2S_3$ Core-shell dual Z-scheme tandem heterojunctions with Broad-spectrum response and enhanced Photothermal-photocatalytic performance. *Chem. Eng. J.* **2022**, *431*, 133355, https://doi.org/10.1016/j.cej.2021.133355.
2. Song, H.; Zhang, Q.; Hu, D.; Sun, Z.; Han, Y.; Meng, H.; Sun, T.; Zhang, X. In-situ partial cation exchange-derived $ZnIn_2S_4$ nanoparticles hybridized 1D MIL-68/$In_2S_3$ microtubes for highly efficient visible-light induced photocatalytic $H_2$ production. *Sep. Purif. Technol.* **2022**, *287*, 120585, https://doi.org/10.1016/j.seppur.2022.120585.
3. Ma, X.; Li, W.; Li, H.; Dong, M.; Li, X.; Geng, L.; Fan, H.; Li, Y.; Qiu, H.; Wang, T. Fabrication of novel and noble-metal-free MoP/$In_2S_3$ Schottky heterojunction photocatalyst with efficient charge separation for enhanced photocatalytic $H_2$ evolution under visible light. *J. Colloid Interface Sci.* **2022**, *617*, 284–292, https://doi.org/10.1016/j.jcis.2022.03.021.
4. Ma, X.; Ren, C.; Li, H.; Liu, X.; Li, X.; Han, K.; Li, W.; Zhan, Y.; Khan, A.; Chang, Z.; et al. A novel noble-metal-free $Mo_2C$-$In_2S_3$ heterojunction photocatalyst with efficient charge separation for enhanced photocatalytic $H_2$ evolution under visible light. *J. Colloid Interface Sci.* **2020**, *582*, 488–495, https://doi.org/10.1016/j.jcis.2020.08.083.
5. Ma, X.; Li, W.; Ren, C.; Li, H.; Liu, X.; Li, X.; Wang, T.; Dong, M.; Liu, S.; Chen, S. A novel noble-metal-free binary and ternary In2S3 photocatalyst with WC and "W-Mo auxiliary pairs" for highly-efficient visible-light hydrogen evolution. *J. Alloy. Compd.* **2021**, *875*, 160058, https://doi.org/10.1016/j.jallcom.2021.160058.
6. Li, X.; Lyu, X.; Zhao, X.; Zhang, Y.; Akanyange, S.N.; Crittenden, J.C.; Zhao, H.; Jiang, T. Enhanced photocatalytic $H_2$ evolution over $In_2S_3$ via decoration with GO and $Fe_2P$ co-catalysts. *Int. J. Hydrogen Energy* **2021**, *46*, 18376–18390, https://doi.org/10.1016/j.ijhydene.2021.03.017.
7. Geng, H.; Ying, P.; Li, K.; Zhao, Y.; Gu, X. Epitaxial $In_2S_3$/$ZnIn_2S_4$ heterojunction nanosheet arrays on FTO substrates for photoelectrochemical water splitting. *Appl. Surf. Sci.* **2021**, *563*, 150289, https://doi.org/10.1016/j.apsusc.2021.150289.
8. Li, Y.; Han, P.; Hou, Y.; Peng, S.; Kuang, X. Oriented $Zn_mIn_2S_{m+3}$@$In_2S_3$ heterojunction with hierarchical structure for efficient photocatalytic hydrogen evolution. *Appl. Catal. B: Environ.* **2018**, *244*, 604–611, https://doi.org/10.1016/j.apcatb.2018.11.088.